AGU PUBLICATIONS

Space Weather

RESEARCH ARTICLE
10.1002/2016SW001566

Key Points:
- Investigation of *E* field influence on GIC from each source current by *B* field inversion
- *E* field of AEJ has more influence than EEJ and RC in their respective regions
- EEJ current strength is the weakest, while the RC is the strongest due to a larger flux of charged particles flowing through it

Correspondence to:
M. Kosch,
mkosch@sansa.org.za

Citation:
de Villiers, J. S., M. Kosch, Y. Yamazaki, and S. Lotz (2017), Influences of various magnetospheric and ionospheric current systems on geomagnetically induced currents around the world, *Space Weather*, *15*, doi:10.1002/2016SW001566.

Received 1 NOV 2016
Accepted 31 JAN 2017
Accepted article online 2 FEB 2017

Influences of various magnetospheric and ionospheric current systems on geomagnetically induced currents around the world

J. S. de Villiers[1], M. Kosch[1,2,3], Y. Yamazaki[2], and S. Lotz[1]

[1]SANSA Space Science, Hermanus, South Africa, [2]Department of Physics, University of Lancaster, Lancaster, UK, [3]Department of Physics, University of Western Cape, Bellville, South Africa

Abstract Ground-based observations of geomagnetic field (*B* field) are usually a superposition of signatures from different source current systems in the magnetosphere and ionosphere. Fluctuating *B* fields generate geoelectric fields (*E* fields), which drive geomagnetically induced currents (GIC) in technological conducting media at the Earth's surface. We introduce a new Fourier integral *B* field model of east/west directed line current systems over a one-dimensional multilayered Earth in plane geometry. Derived layered-Earth profiles, given in the literature, are needed to calculate the surface impedance, and therefore reflection coefficient in the integral. The 2003 Halloween storm measurements were Fourier transformed for *B* field spectrum Levenberg-Marquardt least squares inversion over latitude. The inversion modeled strengths of the equatorial electrojets, auroral electrojets, and ring currents were compared to the forward problem computed strength. It is found the optimized and direct results match each other closely and supplement previous established studies about these source currents. Using this model, a data set of current system magnitudes may be used to develop empirical models linking solar wind activity to magnetospheric current systems. In addition, the ground *E* fields are also calculated directly, which serves as a proxy for computing GIC in conductor-based networks.

1. Introduction

Geomagnetically induced currents (GIC) can occur in ground-based technical networks, such as electric power transmission grids, oil and gas pipelines, telecommunication cables, and railway circuits. Solar events, such as geo-effective coronal mass ejections, create disturbances within the Earth's magnetosphere, which can give rise to geomagnetic storms and substorms. During geomagnetic storms, the compression of the magnetosphere by the solar wind and the interaction of the solar wind with the Earth's geomagnetic field (the *B* field) enhance the currents in both the magnetosphere and the ionosphere [e.g., *Bothmer and Daglis*, 2007]. These currents cause fluctuations in the *B* field on the ground. Rapid changes in the *B* field generate geoelectric fields (*E* fields) that drive GIC in the networks.

Ever since the discovery that the Earth has a magnetic field [*Gilbert*, 1600] basic electromagnetic theory suggests that a current system must be involved in driving this field. Its fluctuations with periods shorter than a day have been connected to various current systems high above the Earth's atmosphere. Each current system has its own geomagnetic signature, and a number of standard geomagnetic indices have been developed to quantify each of these signatures in the field. These individual systems have a unique influence on GIC, via the surface *E* field, in conductor networks in various parts of the world. GIC is known to have caused damage and blackouts in power utility systems [e.g., *Kappenman*, 2007; *Gaunt and Coetzee*, 2007]. Where more than one system is influencing any one particular region, then a superposition of individual signatures will result in a combined effect on GIC in this area [*Anderson et al*., 2006].

1.1. Three Source Current Systems

Our world can be subdivided into seven different regions according to the positions of the separate electrojets. The region of the equatorial electrojet (EEJ) on the magnetic dip equator is called the geomagnetic low-latitude region or equatorial region. The northern and southern regions of the auroral electrojet (AEJ) with the ionospheric end of the field-aligned currents are called the geomagnetic high-latitude auroral regions. Both electrojets are about 100 km above the Earth's surface in the ionosphere, and by spherical geometric arguments their influence only extends 6 to 9° away from their respective positions [*Anderson and Anghel*,

2004, 2002, 2006]. What is not covered by the electrojets is called the north and south polar-cap regions, enclosed by each AEJ, and the north and south midlatitude regions of the Earth, between the EEJ and the AEJ.

The Earth's ring current (RC) is partly responsible for shielding the lower latitudes of the Earth from magnetospheric electric fields. It therefore has a large effect on the electrodynamics of geomagnetic storms. The RC system is 3 to 8 Earth radii distant in the equatorial plane and circulates generally westward. The particles of this region produce a magnetic field in opposition to the Earth's magnetic field and so an observer on Earth would see a decrease in the magnetic field in this area, as captured by the disturbance-storm (*Dst*) index [*Baumjohann and Treumann*, 1996; *Kozyra and Liemohn*, 2003].

The term "auroral electrojet" (or AEJ) is the name given to the large horizontal currents that flow in the *D* and *E* regions of the auroral ionosphere confined to the high-latitude regions (65°N/S). The AEJ was first proposed to exist by *Alfven* [1939, 1940] and modeled by *Bostrom* [1964]. During magnetically quiet periods, the electrojet is generally confined to the auroral oval. However, during disturbed periods, the electrojet increases in strength and expands to both higher and lower latitudes. This expansion results from two factors, enhanced particle precipitation and enhanced ionospheric electric fields.

Equatorial electrojet (EEJ) currents were first reported by *Egedal* [1947] to exist in the equatorial ionosphere when the Huancayo geomagnetic observatory started operations in Peru. The worldwide solar-driven wind results in the so-called *Sq* current system in the *E* region of the Earth's ionosphere (100–130 km altitude). Resulting from this current is an electrostatic field directed east-west (dawn-to-dusk) in the dayside of the ionosphere. At the magnetic dip equator, where the *B* field is horizontal, this electric field results in an enhanced eastward current within ±3° of the magnetic dip equator, known as the EEJ [*Onwumechili*, 1998; *Casey*, 2005].

Recent research focuses on the topic of GICs in low-latitude or equatorial regions. The impact of these currents at high latitudes has been extensively researched, but the magnetic equator has been largely overlooked. In *Pulkkinen et al*. [2012] a series of 100 year extreme *E* field and GIC scenarios are explored by taking into account the key geophysical factors associated with the geomagnetic induction process. *Ngwira et al*. [2013] report on the global behavior of the horizontal *B* field and the induced *E* field fluctuations during severe/extreme geomagnetic events. *Carter et al*. [2015] investigated the potential effects of interplanetary shocks on the equatorial region and demonstrated that their magnetic signature is amplified by the EEJ.

This paper will introduce a new geomagnetic inversion method of a line current model that makes possible the computation of current strengths of the EEJ, the AEJ, and the RC and determination of the separate ground *E* fields that influence and drive GIC in conducting media networks on the ground. We will use the input indices of *EE* (defined by *Uozumi et al*. [2008]), *AO* (defined by *Davis and Sugiura* [1965]), and *Dst* (defined by *Sugiura* [1964] and *Gannon and Love* [2011]) or *SYM-H* (defined by *Iyemori* [1990] and *Wanliss and Showalter* [2006]) for each current system, respectively. We will show that the inversion results compare accurately to the direct results of the forward problem. We base our geomagnetic inversion approach on the line current's *B* and *E* field computations of *Boteler and Pirjola* [1998], *Pirjola and Viljanen* [1998], *Pirjola* [1998], *Boteler et al*. [2000], *Pirjola and Boteler* [2002].

One motivation for using inversion techniques in this study is that the *B* field measurement is generally not available at the location of interest for calculation of the *E* field. *B* field recordings are only made at established observatories and where additional magnetometers were installed. When *E* fields are directly computed from available *B* field data, via ground impedance from an appropriate conductivity profile, this can only be done at those locations. On-site profiles may not even be available at such locations; thus, nearby profiles have to be found and used instead. The inversion method allows one to compute the *B* fields over a range of latitudes along a chosen meridian in the vicinity of these stations. Once the current strength is determined, as an output parameter, one can return to the model function in the forward problem and use the parameter to calculate the *E* fields anywhere other than just at *B* field measurement locations. Inversion provides an alternative way in which to estimate *E* fields where it is not possible by any other means [*De Villiers and Cilliers*, 2014].

2. Background

While *Cagniard* [1953] was the seminal paper that opened the field of magnetotelluric and GIC studies, *Wait* [1958, 1980] introduced the layered-Earth method for computing surface impedances, reflection

coefficients, and related material properties of the ground underneath the Earth. Originally introduced by *Wait and Spies* [1969], *Thomson and Weaver* [1975] applied the complex image method to the induction of line currents in a layered Earth. The beginnings of a theory of *B* fields and *E* fields of line current systems at a distance above the Earth's surface in plane geometry has been researched by *Pirjola* [1982,1984,1985], *Viljanen* [1992], and later *Pulkkinen* [2003]. A comprehensive theory was presented by *Häkkinen and Pirjola* [1986] for computing the *B* fields and *E* fields at the Earth's surface due to an electrojet in the magnetosphere above a layered Earth.

We build on the above theory with a new approach presented by *De Villiers and Cilliers* [2014] and *De Villiers et al*. [2016]. They introduced geomagnetic inversion to obtain ionospheric current system parameters in the frequency ω and latitude x domain. In the former reference, the setup was prepared for a given real-valued spectral current strength $J(\omega)$ at a single frequency ω only, height h, and latitude position x_o. To test that the inversion techniques work, simulated data were generated over x space from the given parameter values and inserted into the inversion setup to recover those parameters. In the latter reference, only the strength of the current was determined with fixed distance parameters ($h \neq 0$, $x_o = 0$) by the same inversion method from measured *B* field data for two stations simultaneously (under and away from the current system). The current strength was complex-valued this time, and each complex part became two independent model parameters, i.e., $J_r(\omega)$ and $J_i(\omega)$. The inversion was repeated for the range of frequencies determined from a Fourier transform of the given measurements.

The above methods were then adapted to this paper's approach described below. Source currents can still be approximated with a line current system. Each current system is now associated with only one appropriate geomagnetic index. The geomagnetic horizontal component B_x is normally assigned to the index. No additional independent geomagnetic index is available for the inversion. This makes the inversion underdetermined with two model parameters and only a single Fourier transformed data point of the index, assumed to be located directly underneath the source current. The procedure has to be adapted by generating at least one more set of data from the same index and positioned away from the system. With two mutually dependent data points at different locations sufficient for the inversion to be well determined, perfect convergence results and the two parameters are determined exactly.

The Fourier integral of the *B* field extended for field observations above or below the Earth's surface:

$$\begin{bmatrix} B_x \\ B_z \end{bmatrix}(x,z,\omega) = \frac{\mu J(\omega)}{2\pi}\int_0^\infty \begin{Bmatrix} [R(v,\omega)+1]\cos(vx) \\ [R(v,\omega)-1]\sin(vx) \end{Bmatrix} e^{-v(z+h)}dv. \quad (1)$$

where $R(v,\omega)$ is the surface reflection coefficient and v is the horizontal wave number. Only surface *B* fields ($z = 0$ km) are evaluated and only the B_x component will be used as the input model function for the inversion process in this study. In general, the integrals involved have no analytical solutions and must be solved numerically.

3. Methods and Procedures

The source currents can be approximated by a line current physical system described in the previous section. Geomagnetic data are obtained in the form of indices for each current system: *AO* for the AEJ, *EE* for the EEJ, and *Dst* or *SYM-H* for the RC. The *AO*(=½ *AU* + ½*AL*) index is preferred to the *AE*(=*AU* − *AL*) index since it represents the equivalent current for the auroral zone and not just the net effect of the eastward and westward electrojets. Then a geomagnetic least squares inversion is done by fitting the model function to the input index, determining the current strength as an output model parameter of the function, with the sum-of-squared residuals as objective function. The current strength parameter can then be used to calculate the *E* field on the Earth's surface directly underneath the current system. The *E* field is responsible for driving GIC in conductor networks in a given region. Computation of GIC is outside the scope of this work, as it requires knowledge of grounded conductor network parameters.

We choose to analyze the Halloween Storm of the year 2003. This is a widely studied event with known GIC-related impact on networks at middle latitudes [e.g., *Love and Swidinsky*, 2015; *Torta et al*., 2012; *Pulkkinen et al*., 2012; *Gaunt and Coetzee*, 2007; *Trivedi et al*., 2007].

Table 1. Locations of Two Stations and Three Conductivity Structures on Three Continents[a]

	Coordinates (Zero Altitude Assumed)		
Place Name	Geographic	Geomagnetic[a] (IGRF 2005)	Apex[b] (Year 2003.833)
Addis Ababa, Ethiopia	9.03°N, 38.77°E	5.26°N, 111.70°E	[0.5528°N, 0.5532°N], 111.61°E
Huancayo, Peru	12.05°S, 75.33°W	1.74°S, 3.45°W	[0.5308°N, 0.5312°N], 3.51°W
Quebec, Canada	53.75°N, 71.98°W	63.82°N, 0.24°W	[63.1673°N, 63.1798°N], 7.44°E
Nairobi, Kenya.	1.27°S, 36.80°E	4.50°S, 108.11°E	[11.1327°S, 11.1386°S], 109.80°E
Tocopilla, Chile.	22.10°S, 70.20°W	11.72°S, 1.52°E	[9.3586°S, 9.3636°S], 0.95°E

[a]Apex format (MagApex-Latitude; QuasiDipole-Latitude), MA/QD-Longitude.
[b]From http://wdc.kugi.kyoto-u.ac.jp/igrf/gggm/index.html.
[c]From http://ccmc.gsfc.nasa.gov/coord_transform/index.php;. Source *Richmond* [1995].

Data of *AO*, *Dst*, and *SYM-H* are already available on the Kyoto Space Weather Centre website. However, the *EE* index, used as a measure of the zonal current intensity of the EEJ, only started data records in the year 2010 and are thus unavailable for the storm in question. The index represents horizontal magnetic perturbations at the magnetic equator corrected for the *Dst* index. We derived the *EE* index separately for the African and American sectors by using magnetic measurements from 26 October to 7 November 2003 at the INTERMAGNET stations [*Kerridge*, 2001] Addis Ababa (Ethiopia) (International Association of Geomagnetism and Aeronomy (IAGA) code AAE) and Huancayo (Peru) (IAGA code HUA), respectively (see Table 1 for the coordinates). *Dst* minute data were taken from the United States Geological Survey (USGS) website. Therefore $EE(t) = \Delta B_x(t) - Dst(t)$ where $\Delta B_x(t) = B_x(t) - \text{median}(B_x(t))$. The median of *B* field measurements was taken for the entire 13 day period.

Surface impedance and reflection coefficient data can be derived from conductivity profiles of the ground. For the EEJ, the nearest available profile to Ethiopia is taken to be in Nairobi, capital of Kenya, and was simplified from a more complete profile given in the Appendix. The nearest available profile to Peru [*Schwarz and Kruger*, 1997, Figure 7a] is on strip A across northern Chile at 21.5°S. We take the structure where this strip meets the Pacific coast, at Tocopilla harbor. The profile is named after this harbor town, as it is not named in the given reference (see Table 1 again for the coordinates). A deep-layer conductivity profile was also derived from Swarm satellite geomagnetic measurements [*Civet et al*., 2015] and appended to the Nairobi and Tocopilla profiles from below. Table 2 lists the conductivities and thicknesses of the profiles. The Quebec conductivity profile [*Boteler and Pirjola*, 1998] was used for the AEJ *E* field. The Swarm conductivity profile alone was sufficient to compute the RC *E* field.

3.1. Forward Computation of Line Current Systems

From equation (1) the *B* field north component is restated here for the forward problem [*Häkkinen and Pirjola*, 1986; *Boteler et al*. 2000].

Table 2. Parameters of 1-D Approximation to Ground Conductivity Structure[a,b]

Locations →	*Nairobi [Modified]*		*Tocopilla*		*Swarm Satellite*	
Layers ↓	Thickness (km)	Conductivity (mS/m)	Thickness (km)	Conductivity (mS/m)	Thickness (km)	Conductivity (mS/m)
Layer 1	5	12.6	6	20.0	400	1.0
Layer 2	15	18.9	2	12.5	100	1.4
Layer 3	60	33.6	17	20.0	100	2.7
Layer 4	20	63.2	20	0.2	50	5.2
Layer 5	60	22.4	25	2.0	50	14.4
Layer 6	100	17.2	30	0.2	50	27.0
Layer 7					50	100
Layer 8					50	280
Layer 9					50	1050
Layer 10					350	2700
Layer 11					750 (∞)	3745

[a]The structure for Quebec is given in *Boteler and Pirjola* [1998].
[b]It is based on magnetotelluric measurements at two locations and a satellite.

$$B_x(x,\omega) = B_{x,r}(x,\omega) + iB_{x,i}(x,\omega) = \frac{\mu}{2\pi}\int_0^\infty J(v,\omega)[R(\omega)+1]e^{-vh}\cos(vx)dv \tag{2}$$

Note that for purposes of this discussion, the current strength $J(\omega)$ was generalized for a latitude distributed current system and incorporated into the integral. This is easily computed provided that the current strength $J(v,\omega)$, reflection coefficient $R(\omega,v)$, and fixed distance parameters (h,x) are known. However, if the $J(v,\omega)$ is unknown, then equation (2) must be determined from ground geomagnetic measurements instead. The current strength is still inside the integral and cannot be separated from the integral while it still depends on the integration variable v (i.e., it is integrated along with the rest of the integrand). Inversion alone will have to be applied to fit the right-hand side of equation (2) model function to a Fourier transform of the left-hand side of equation (2) geomagnetic measurements.

Line current systems make the forward problem easier, because then $J(v,\omega) \rightarrow J(\omega)$ and the current strength can be taken out of the integral. With $J(\omega)$ separated, we define a new function for the remaining integral:

$$F_x(x,\omega) = F_{x,r}(x,\omega) + iF_{x,i}(x,\omega) = \frac{\mu}{2\pi}\int_0^\infty [R(\omega,v)+1]e^{-vh}\cos(vx)dv \tag{3}$$

Equation (2) then becomes $B_x(x,\omega) = J(\omega)F_x(x,\omega)$, and dividing through by equation (3) gives

$$J(\omega) = J_r(\omega) + iJ_i(\omega) = \frac{B_x(x,\omega)}{F_x(x,\omega)} = \frac{F_x^*(x,\omega)B_x(x,\omega)}{|F_x(x,\omega)|^2} \tag{4}$$

allowing the current strength to be determined by forward calculation. All that remains then is to take the inverse Fourier transform of $J(\omega)$ to obtain time series data $J(t)$ for the storm period.

3.2. Inverse Modeling of Line Current Systems

The $B_{x;n} = B_x(x_n,\omega)$ is the given data points at positions x_n, $n = 1, \ldots, N$, and equation (2) is used as the model function $B_x(x,\omega)$ for the adapted inversion problem [*De Villiers et al.*, 2016]. The inversion is a least squares problem where the objective function is the sum-of-squared residuals, $\mathrm{SSR} = \sum {r_n}^2$, where $r_n = B_x(x,\omega) - B_{x;n}$. Various optimization techniques are used to minimize the SSR in order for equation (2) to be fitted to the given data. One technique robust enough for this task is the Levenberg-Marquardt method [*Press et al.*, 1992; *Lourakis*, 2005].

The model function is fitted to a set of input data points from the geomagnetic measurement transform at different latitude positions along the meridian. To simplify calculations, the origin of the x space is always underneath the respective latitude position of each current system. On this latitude space, the inversion is repeatedly run for each frequency of the resulting measurement spectrum, each complex value fitted to the model function and the output model parameters determined. For all given frequencies therefore a parameter spectrum of amplitudes is set up.

As per definition, the model function must contain output model parameters which can be adjusted by the inversion in order for the model function to best fit the given data. These parameters are derived from two distinct elements of the physical setup: the thicknesses and conductivities of layered-Earth profiles, and the current strength and distance positions (height and latitude) of the line current system. When only the current strength is adjusted, the inversion is a linear problem (the aim for this paper). When any of the other parameters are adjusted, with or without the current strength, the inversion becomes nonlinear.

Figure 1 shows a diagram of the geomagnetic inversion over latitude space for only a single frequency representing either the real or complex part of the B field measurement transform. Only one diagram is shown; the other diagram of the pair is similar. The plot consists of a bell-shaped inversion model function (solid curve) and three data points (circles). This setup will be used in all our line current inversion computations.

In the plot, the recorded index is to be associated with the central data point at the relevant current system position, i.e., $B_{\mathrm{index}} = B_x(x=0,\omega)$. This is also the maximum of the curve in Figure 1. However, the inversion cannot work with just one given data point (i.e., it is underdetermined and ill-defined). It becomes necessary to strengthen the setup with at least two data points. For this to be done, first the forward calculation in

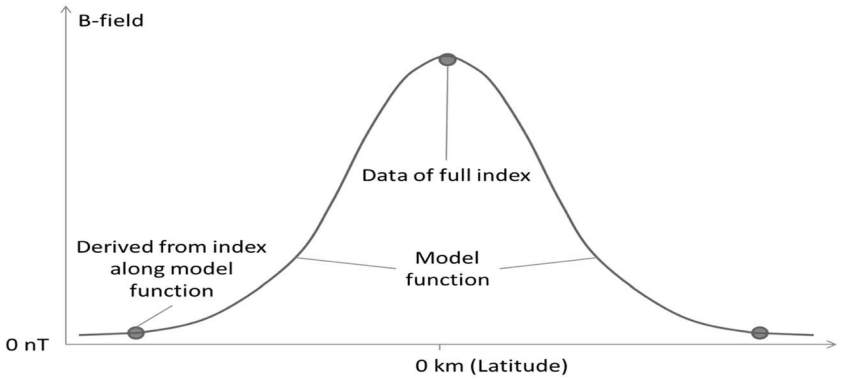

Figure 1. A diagram of the least squares residual inversion problem. A residual is the difference between the data (circle) at a point and the model function (curve) value at that point. The "data of full index" (i.e., *Dst*) is at the origin of latitude, the position of the current system. The data "derived from index along model function" are symmetrically placed around the origin.

equation (4) is used to obtain the current strength: $J(\omega) = B_x(0, \omega)/F_x(0, \omega)$. Second the computed $J(\omega)$ is substituted into equation (2) for calculation of $B_x(x \neq 0, \omega)$. Then inversion can proceed.

Though not a requirement for inversion, the model function is also symmetric around $x = 0$ km. It is then possible to compute one data point at $x = x_s$ on one side of the current system. By symmetry, $B_x(-x_s, \omega) = B_x(+x_s, \omega)$ is computed for equal and opposite position $x = -x_s$ on the other side. This then defines two symmetric data points $B_x(\pm x_s, \omega)$ that anchor the central data point $B_x(0, \omega)$. We use these three input data points (thus $N = 3$) from only one measured geomagnetic data set (i.e., the index) to perform the inversion in this paper.

3.3. *E* Field Calculation

The *E* field is important because it is regarded as the main driver for creating GIC in conductor networks on the surface of the Earth. There are two equally valid formulations:

1. The integral way is the calculation of the *E* field from the given current system and the surface impedance via the surface reflection coefficient $R(v, \omega)$, without recourse to measured *B* fields beforehand. The *E* field Fourier integral [*De Villiers et al*., 2016] is

$$E_y(x, \omega) = i\omega \frac{\mu_0 J(\omega)}{2\pi} \int_0^\infty [R(v, \omega) - 1] v^{-1} e^{-vh} \cos(vx) dv. \tag{5}$$

For $R(v, \omega) = \frac{i\omega\mu_0 - vZ(\omega)}{i\omega\mu_0 + vZ(\omega)}$, the field calculations give the same results in the integral method at the position ($x = 0$ km) of the current system, as those computed from the direct method. The surface impedance $Z(\omega)$ is embedded in the reflection coefficient and computed from ground profiles.

2. The direct way is to calculate the ground *E* field from the ground *B* field by multiplying it by the surface impedance $Z(\omega)$, where the free space permeability constant is μ_0:

$$E_y(x, \omega) = -\frac{Z(\omega)}{\mu_o} B_x(x, \omega). \tag{6}$$

This equation is derived by substituting the expression of $R(v, \omega)$ into equation (5) and recovering the top vector component of equation (1) by separating $Z(\omega)/\mu_o$ from the resulting integral.

An *E* field spectrum is set up by either method for latitudes $x \in [-x_s, 0, +x_s]$. Either way, the results will be the same and its spectrum is then inversely Fourier-transformed to the time series *E* field for the same period of the chosen storm.

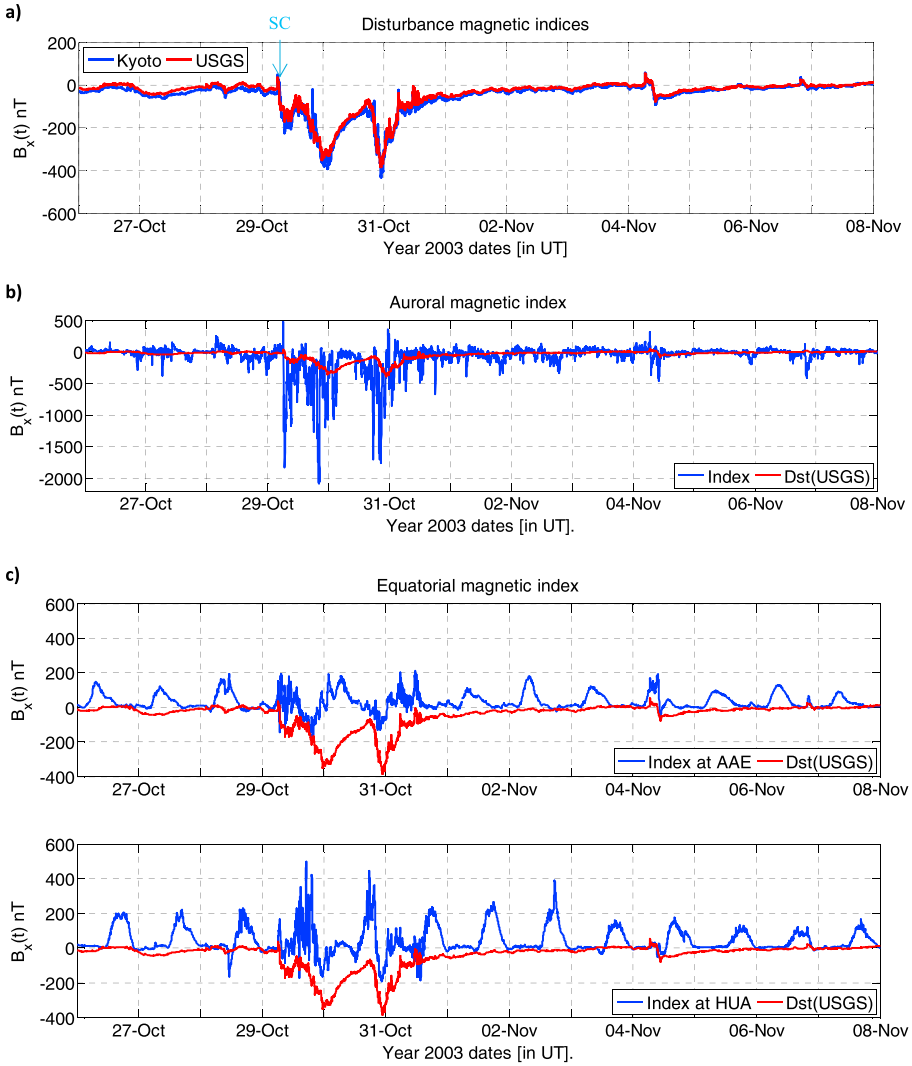

Figure 2. (a) Geomagnetic *Dst* index measurements given by USGS and Kyoto for the RC. The Kyoto index is the min-sampled *SYM-H* data, not the Kyoto hourly *Dst* samples. (b) Geomagnetic *AO*-index derived by Kyoto from northern polar stations for the AEJ current system. The *Dst* index from USGS is also included for comparison. (c) Geomagnetic *EE* indices created by subtracting the *Dst* index of the USGS from the (top) Addis Ababa (AAE) and (bottom) Huancayo (HUA) geomagnetic measurements for the EEJ current system. The *Dst* index from USGS is also included for comparison.

4. Computations and Their Results

4.1. Placement of the Current Systems

E field values are being calculated for three different heights: $h = 100$ km for the AEJ and EEJ and $h = 3R_E$ and $h = 8R_E$ for the RC (Earth's radius: $R_E = 6371.2$ km). For $h = 100$ km, the nonzero symmetric data points are selected to be 6° latitude (or $x_s = 667$ km) away on either side of the AEJ and EEJ. This latitude value is at or near the outer extent of their range of influence, allowing the inversion setup to capture most of the magnetic signatures of the electrojets.

The RC physical setup is more complicated, because of its placement in the upper magnetosphere. Its *B* field is superimposed upon by the geomagnetic signatures from both electrojets in the low and high latitudes. To escape the electrojets' influence, one needs to enter the middle latitudes. The midlatitude region is exposed only to the influence of the RC (and other upper magnetosphere current systems) during a geomagnetic storm. For this reason, the *Dst* is computed from geomagnetic midlatitude stations only (with the EEJ influence thus removed), and then normalized to become an equatorial index [*Sugiura*, 1964]. In our approach then, the index is positioned on the geomagnetic equator underneath the RC.

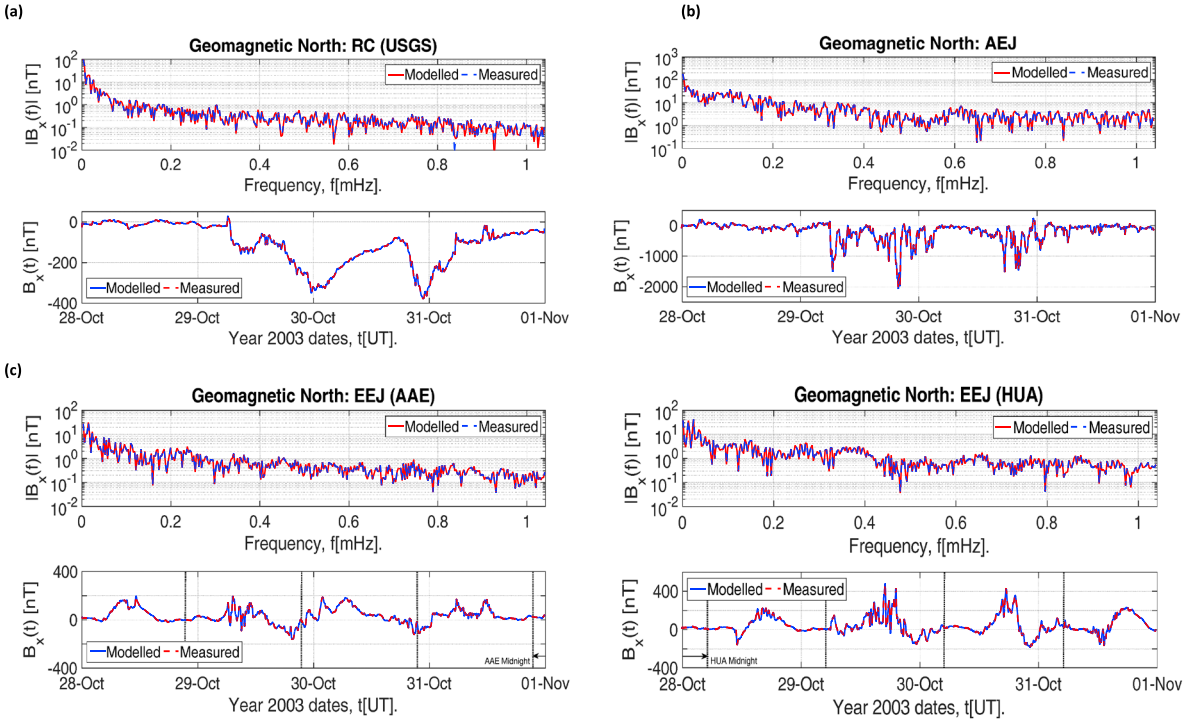

Figure 3. (a) Modeled geomagnetic field directly under AEJ after the *AE* inversion. The solid curves are the model results; the dashed curves are measured data. Geomagnetic field directly under RC after the *Dst* inversion for height three Earth radii above surface, and re-used again for height eight Earth radii. Only the USGS-*Dst* was used. The solid curves are the model results; the dashed curves are measured data. (b) Modeled geomagnetic field directly under AEJ after the *AO* inversion. The solid curves are the model results; the dashed curves are measured data. (c) Modeled geomagnetic field directly under EEJ after the *EE* inversion for (left) AAE and (right) HUA. AAE midnight is 2.6 h ahead of UT, while HUA midnight is 5 h behind UT. The solid curves are the model results; the dashed curves are the measured data.

The index is used for the forward computation of its current strength at this central location. For the inverse computation, a different pair of latitudes is computed to position the symmetric data points on either side of the RC. Due to its height being so far from the Earth, the range of influence of the RC nearly covers all geomagnetic latitudes of the Earth. In RC-Earth spherical geometry, this latitude is calculated from a triangle with the RC-to-Earth's center distance at the hypotenuse and the Earth's radius at the adjacent side. Thus, for the upper height, we have $\cos^{-1}[1R_E/(1+8)R_E] = 83.62^0$ (or $x_s = 9291$ km) north and south of the geomagnetic equator. With this setup, inversion can be applied to the RC as well.

It can be shown that since the same *Dst* (USGS) will be used for the RC at two different heights, then by equation (6) above, the corresponding *E* field derived from the *Dst* (and its subsequent influence on GIC in the midlatitudes) will also be independent of the RC height. When expressing the *Dst* by Fourier integral expressions instead, in the form $B_x(x,\omega) = J(\omega)F_x(x,\omega)$, then equations (3) and (4) applies. Only equation (3) (i.e., $F_x(x,\omega)$) contains the height parameter ($\propto e^{-\nu h}$ inside the integral). With the same *Dst* index used on the RC system, the current strength in equation (4) [i.e., $J(\omega)$] must evaluate as an inverse of $F_x(x,\omega)$. For different given heights in $F_x(x,\omega)$, this scenario suggests a dependence $J(\omega) \propto e^{\nu h}$. However, this latter proportionality is not so simple, as the original exponential must still be evaluated over an integration range of wave number values ν in $F_x(x,\omega)$. Instead, the two given RC-heights are substituted in the exponential, the $F_x(x,\omega)$ integral is computed in each case, and the corresponding current strength values are obtained. Taking the scaling factor then gives $\frac{J(\omega)|_{h=8R_E}}{J(\omega)|_{h=3R_E}} = \frac{F_x(x,\omega)|_{h=3R_E}}{F_x(x,\omega)|_{h=8R_E}} = 338$.

4.2. Input/Output Data and Their Spectrums

Figure 2 gives the 1 min sampled geomagnetic indices (*SYM-H* from Kyoto, *Dst* from USGS, and the polar *AO* and equatorial *EE* for two stations) for the period from 26 October 2003 to 7 November 2003. A major disturbance can be seen on a 3 day storm period (29–31 October 2003), namely, the geomagnetic Halloween Storm. Its sudden commencement starts at 06:14 on the first morning. We narrow the period to between

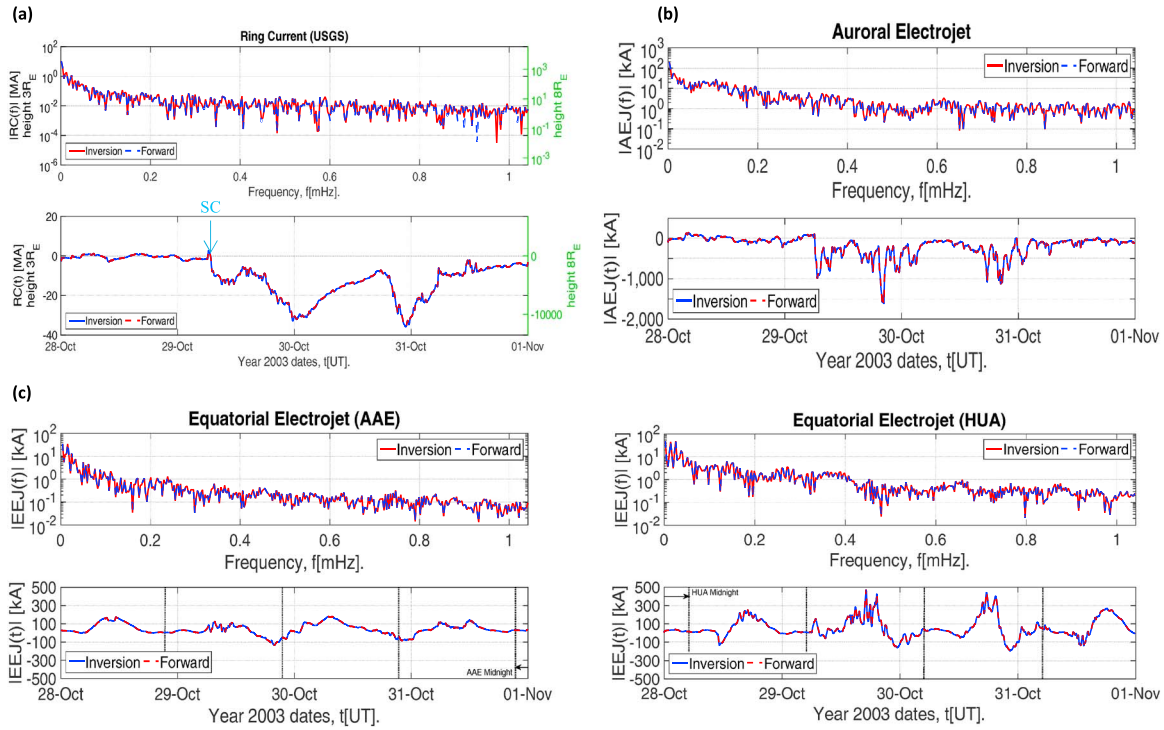

Figure 4. (a) RC current by geomagnetic *Dst*(USGS) inversion for three (black left axes) and eight (green right axes) Earth radii height above surface. The solid curves are the model results; the dashed curves are computed from the measured data. (b) AEJ current by geomagnetic *AO* inversion. The solid curves are the model results; the dashed curves are the measured data. (c) EEJ current by geomagnetic *EE* inversion from (left) AAE and (right) HUA. AAE midnight is 2.6 h ahead of UT, while HUA midnight is 5 h behind UT. The solid curves are the model results; the dashed curves are the measured data.

28 October and 1 November 2003 and compute their Fourier transforms. A Brickwall low-pass filter [*Owen*, 2007: p. 81] is applied on the Fourier transformed data. The amount of radiation energy allowed to pass through (at the threshold cutoff frequency an eighth of Nyquist frequency (8.33 MHz)) is given as a percentage of the total sum of the spectrum (*Dst*(USGS): 82%, *AO*: 64%, *EE*(AAE): 61%, and *EE*(HUA): 66%).

When the inversion procedure is run, the geomagnetic model is fitted to the transformed data of a given index at each frequency from 0 to 1.04 MHz of the spectrum incremented over 360 points (an eighth of 4 days times 1440 min/d), and the data shown are that at the central position of the current system involved. Figure 3 shows a comparison of the modeled and measured data for all the indices in both the frequency and time domains. A cross correlation between the modeled and measured sets should approach autocorrelation of either set, if the two sets are the same (i.e., a symmetric function around zero lag). This can be checked by determining not only the lag position of maximum cross correlation but the root-mean-square (RMS) of the differences between symmetric pairs outward around that lag position. For all the current systems concerned, both the lag and RMS values are found to be zero. The modeled signatures are virtually on top of the measurements. This indicates that the model is correct and complete resulting in a perfect fit to the measured data (with zero residuals in the SSR). This can also be independently confirmed in the subsequent figures below.

Figure 4 shows the current strengths of the three source current systems and its output spectrums obtained from inversion of the three respective geomagnetic indices. While the corresponding current strengths depend on the two different heights of the RC, this is indicated on both vertical axes on either side of the plots in Figure 4a. A sudden commencement of the geomagnetic storm is visible in the RC current strength. The AEJ strength shows more rapid fluctuations than the RC throughout the 4 day period. The EEJ strengths do not follow the storm patterns seen in both AEJ and RC (i.e., deep negative values of the main phase) but are nevertheless disturbed by rapid fluctuations of the storm. These fluctuations distort, but do not destroy, the diurnal strength at both given stations. The HUA diurnal strength is stronger than that of AAE. For each station, local midnight (UT-2.6 h for AAE and UT + 5 h for HUA) is indicated by vertical lines in the plots.

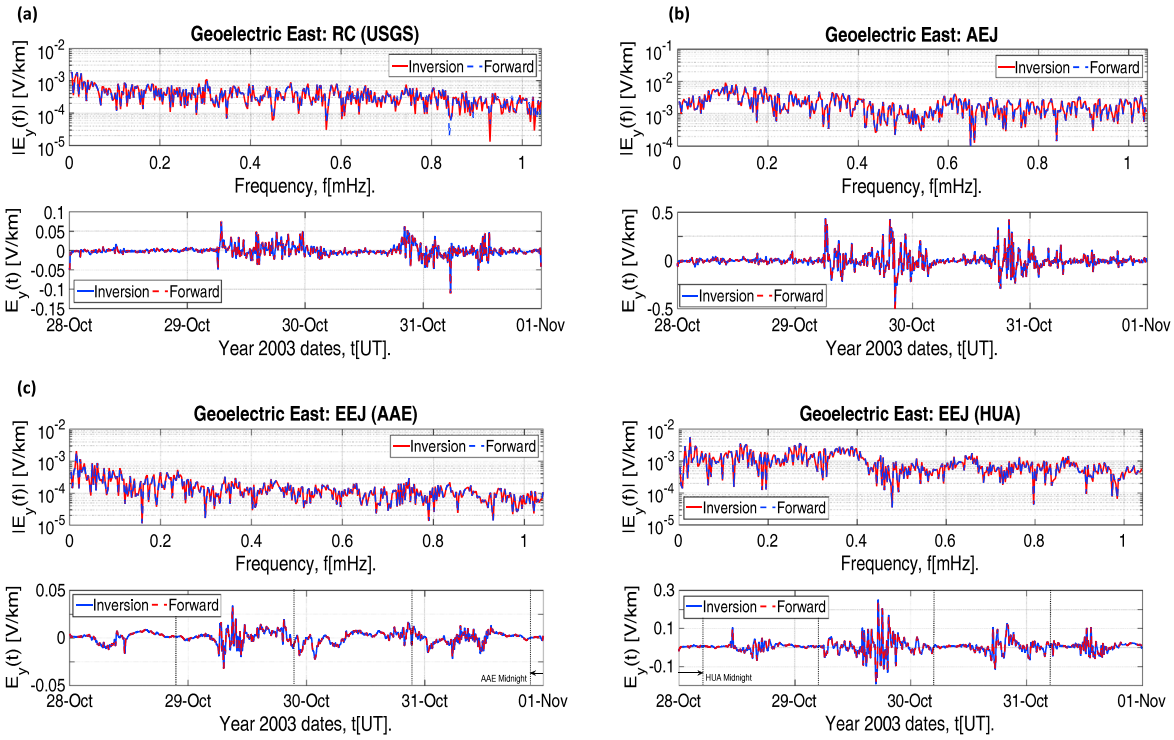

Figure 5. (a) Geoelectric field directly under RC after the *Dst* inversion independent of the height above the surface. The USGS-*Dst* was used. The solid curves are the inverted results; the dashed curves are the forward computed data from *Dst* measurements. (b) Modeled geoelectric field directly under AEJ after the *AO* inversion. The solid curves are the model results; the dashed curves are the measured data. (c) Modeled geoelectric field directly under EEJ after the *EE* inversion for (left) AAE and (right) HUA. AAE midnight is 2.6 h ahead of UT, while HUA midnight is 5 h behind UT. The solid curves are the model results; the dashed curves are the measured data.

Figure 5 shows the *E* fields associated with each index that is computed for the three source current systems. During the given 4 day period, all the *E* fields show two distinct periods of strong activity, and an intervening calm period. For the AEJ, the *E* field appears more stable than the corresponding fields of the other current systems due to a flat trend with small fluctuations around 0 V/km in the quiet times. In the disturbed times, the AEJ *E* field fluctuates with the greatest range than the other current systems, ± 0.5 V/km. At AAE, the *E* field of the EEJ is around 10 times weaker than the AEJ *E* field, ± 0.05 V/km. At HUA, the *E* field of the EEJ is stronger and shifted, [−0.2, + 0.3] V/km (half the range of the AEJ *E* field). This is even twice as strong as the RC *E* field at [−0.15, + 0.1] V/km.

With the correct model, the *E* fields can be determined through the conductivity profile. Traditionally, in the frequency domain and on the surface, the *E* field components are directly related to the *B* field components via the profile's impedance, see equation (6). However, the *E* fields can also be obtained via equation (5), involving a current density function and a reflection coefficient, the latter of which contains the same surface impedance spectrum. Via $i\omega J(\omega) \leftrightarrow \partial J(t)/\partial t$, the *E* field is shown in the figures to be directly related to the rate of change of currents over time. For rapid *B* field changes, this shows up as large spikes that can generate GIC impulses down a line segment of the conductor networks over a given area.

As a consequence of height independence of the *Dst* index and its *E* field, only one transform and its time series is shown in Figure 3a (*Dst*) and Figure 5a (*Dst E* field). By contrast, Figure 4a (currents) shows two transforms and its time series on either vertical axes of the plots, corresponding to two different RC heights.

5. Discussion

The Spherical Elementary Current Systems (SECS) method was introduced by *Amm and Viljanen* [1999]. A matrix of such systems in the ionosphere is set up over a surface coordinate grid of positions in any given region where a power network resides [e.g., *Pulkkinen et al.*, 2003; *Wik et al.*, 2008]. A geomagnetic model

function is fitted to known geomagnetic measurements at selected observatories in this region, using any decomposition inversion technique, with the currents as linear output parameters. *Vanhamäki et al*. [2003] developed a one-dimensional version of SECS and found it to be 5–10% in error compared with the original two-dimensional SECS in real situations. *Viljanen et al*. [2004] applied the method in GIC studies in Finland by using a plane-Earth layered model of conductivities and found that a simple plane wave model is fairly accurate compared to GIC measurements. A Cartesian Elementary Current Systems version has also been developed [*Vanhamäki and Amm*, 2007]. This interpolation method is best suited for determining all source current systems over a two-dimensional (2-D) ionospheric surface (without distinction between the AEJ, EEJ, and even the Solar-quiet system) above and in parallel with the Earth at any instant in time.

Our inversion approach is more apropriate to the simpler setup of line currents systems (applied in turn to RC, AEJ, and EEJ as physical systems) and generates current strength data at a single location for a set of geomagnetic measurements over a given period. The advantage over SECS is that this simplified inversion method provides only two linear output parameters $J_r(\omega)$ and $J_i(\omega)$ of the current strength (see equation (4)) of the line current system, while SECS requires many current strength output parameters (the complex parts for two horizontal components, $J_{x,y}(\omega)\big|_{(x_n,y_m)}$ at every coordinate grid point (x_n, y_m)).

5.1. Recent GIC Research

Pulkkinen et al. [2012] specifically derive explicit *E* field temporal profiles as a function of ground conductivity structures and geomagnetic latitudes. They also demonstrate how extreme *E* field scenarios can be mapped into GIC. Generated statistics indicate 20 V/km and 5 V/km 100 year maximum 10 s *E* field amplitudes at high-latitude locations with poorly conducting and well-conducting ground structures, respectively. They show that there is an indication that *E* field magnitudes may experience a dramatic drop across a threshold latitude boundary at about 40–60° of geomagnetic latitude. Below the boundary (equatorward) the *E* field magnitudes are about an order of magnitude smaller than those above the boundary (poleward).

Ngwira et al. [2013] work on the *B* field behavior, and the *E* field fluctuation it induces during severe geomagnetic events includes (1) an investigation of the latitude threshold boundary, (2) the local time dependency of the maximum induced *E* field, and (3) the influence of the EEJ current on the occurrence of enhanced induced *E* fields over ground stations located near the dip equator. Using ground-based and the Defense Meteorological Satellite Program measurements, they confirm that the latitude threshold boundary is associated with movements of the auroral oval and the corresponding AEJ, which is the main driver of the largest perturbations of the ground *B* field at high latitudes. In addition, they show that the enhancement of the EEJ is driven by the penetration of high-latitude *E* fields and that the induced *E* fields at stations within the EEJ can be an order of magnitude larger than that at stations outside the EEJ.

Our results confirm the studies of *Pulkkinen et al*. [2012] and *Ngwira et al*. [2013]. The *E* field due to the AEJ is many times stronger than the RC, and its effects on GIC are taken more seriously (as evidenced by the March 1989 Quebec power blackout event [*Beland and Small*, 2004]). The same is true of the southern high-latitude region; though in Antarctica no conducting infrastructures exist over large areas. The southern AEJ also moves into the midlatitudes during major disturbances, as evidenced by significant GIC and the damage it caused in South Africa [*Gaunt and Coetzee*, 2007] and New Zealand [*Marshall et al*., 2012].

In *Carter et al*. [2015], the local amplification of the EEJ magnetic signature is shown to substantially increase the equatorial region's susceptibility to GICs in the presence of interplanetary shocks. Importantly, this result applies to both geomagnetic storms and quiet periods and thus represents a paradigm shift in our understanding of adverse space weather impacts on technological infrastructure. In addition, it is shown that the amplification is larger at Huancayo (HUA) than that at Addis Ababa (AAE) and that this difference may be attributed to geological differences on the two continents.

By comparison, our results show that the EEJ is both weaker (at AAE) and stronger (at HUA) than the background RC. An amplified *E* field is superpositioned onto the *E* field of the RC at both stations for a combined effect on GIC in the magnetic dip equator region. GIC effects in the low-latitude and midlatitude regions, however, are the lowest and affected by the RC alone.

5.2. Behavior of the *B* Fields, *E* Fields, and Source Currents

The *B* field index of each current system exhibits different characteristic behaviors that identify the different geomagnetic signatures. As such, the strength of the current systems also behaves differently from each other, with similar characteristics to those of the *B* field. By contrast, the *E* field exhibits behavior that is different from that seen in the computed *B* field and current strength. In Figure 5, the *E* field appears to vary as the time rate of change of the *B* field and current strength in each system; while in Figure 4, the current strengths vary as that of the *B* field indices (Figure 3).

For the RC (Figure 3a), and more rapidly the AEJ (Figure 3b), the *B* field measurement data show a sudden commencement marking the initial phase of the geomagnetic storm. Not long after, the field decreases substantially from its quiet time variations around zero magnetic value, introducing the main phase of the storm. After reaching a deep minimum, it gradually returns to the normal quiet time values in the recovery phase. In the EEJ (Figure 3c), this behavior is absent and only the rapid fluctuations are left to mark the presence of a storm, as distinct from the smooth variations of the quiet times. Correspondingly, these different storm characteristics are also strongly reflected in the current strength values among the current systems.

Corresponding to the *B* fields, the *E* fields show a characteristic amplitude modulation of its oscillatory behavior that can only be part of the main phase of the storm under all the systems concerned. The *E* field is the driver for GIC on the ground and contains spikes that translate into impulses of the GIC being sent down the conducting infrastructures and that could potentially damage them. In the quiet times, however, (Figure 5: around 04:00–18:00 on 30 October 2003, before 06:00 on 29 October 2003, and after 14:00 on 31 October 2003), these oscillations are so small that the *E* fields may be considered to have vanished, with no concern for the infrastructures involved.

5.3. *E* Fields on GIC

The horizontal vector *E* fields drive GIC in any conductor network on the ground. Computed from network circuitry parameters, the GIC would likely follow the changes of a projected *E* field along any one path of the network, with a good correlation. However, within the scope of this study, only line currents in the east/west (or *y*) direction are considered; therefore, only E_y can be computed that is parallel to it. No *E* field north component was involved, which therefore limits the GIC computation only in the east direction. Equation (1) of *Pulkkinen et al*. [2007] is adapted by removing the north *E* field component term but keeping the east *E* field component term: $GIC(x,t) = bE_y(x,t)$. The GIC is now directly proportional to the *E* field east component, with *b* as proportionality coefficient. In the absence of available GIC recordings, no *b* can be computed; thus, a value must be chosen for it. This was determined in the given reference to be of the order of tens of ampere-kilometer per volt. One typical value we choose would be 50 A · km/V. The maximum *E* field range seen in Figure 5 is that of the AEJ. Multiplying the *E* field range with the coefficient gives $GIC \epsilon [\pm 25]$ A. For the EEJ at Addis Ababa (AAE), the GIC is smaller by 10 times. For the EEJ at Huancayo (HUA) it is $GIC \epsilon [-10, +15]$ A. For the RC we have $GIC \epsilon [-7.5, +5.0]$ A. This supports previous research that conductor networks in auroral regions are at greatest risk of generating large GIC than networks in the rest of the world. For example, *Danskin and Lotz* [2015] show that auroral regions are more prone to extreme events and *Thomson et al*. [2011] also refer to the latitudinal dependence of extreme GIC. See *Ngwira et al*. [2013], *Pulkkinen et al*. [2012] (already cited), and the references within.

While calculations of *Barbosa et al*. [2015] and *Trivedi et al*. [2007] only produced 10 A in GIC (for an *E* field value: ~ 500 mV/km) in Brazil during the November 2004 geomagnetic storm, *Barbosa et al*.'s [2015] model also estimated a value of 25 A (*E* field: ~ 900 mV/km and d*B*/d*t*: ~ 116 nT/min) in South Africa during the Halloween Storm of 2003. *Gaunt and Coetzee* [2007] have already linked GIC as a likely cause to South African transformer damage at that time. While GIC values are usually in the order of tens of amperes, in Sweden *Wik et al*. [2008] report (to our knowledge) the largest GIC ever recorded on a power transmission line: 300 A at Simpevarp-2 power substation on 06 April 2000 (where a d*B*/d*t* value of around 500 nT/min was recorded at Brorfelde nearby). For this GIC record, a possible estimate of an *E* field could be 4000 mV/km. However, Sweden is in the auroral zone. In the midlatitude region, *Watari et al*. [2009] and *Watari* [2015] only report a maximum GIC of 3.85 A (*E* field value: ~ 40 mV/km and d*B*/d*t* value: ~ 0.235 nT/s

(or ~14 nT/min.)) at Memanbetsu magnetic station in Japan during a moderate storm on 14–15 December 2006.

The GIC would likely also change in relative proportion to the time rate of change of the *B* fields and the currents (via the *E* fields). When a sudden commencement occurs, marking the start of a geomagnetic storm, the sudden change in the horizontal *B* field would create spikes in the perpendicular horizontal *E* field that will send corresponding impulses of GIC through a conductor path. Such impulses may cause damage or malfunction to any particular piece of equipment or component parts of the conductor network [*Barbosa et al*., 2015; *Zhang et al*., 2015; *Liu et al*., 2014; *Pulkkinen et al*., 2012; *Thomson et al*., 2005, Figure 3].

The optimal operation of equipment and related components is essential to the operation of conducting infrastructure; therefore, mitigation of GIC effects are critical. GIC can be computed and therefore predicted; therefore, comprehensive warning systems are being developed to assist these utilities in taking preemptive measures to minimize or avoid any damages and other consequences to the public.

6. Summary

In this paper, a simplified field inversion setup is used in which ionospheric line currents are computed from *B* field observations on the ground. From these currents, we estimate the induced *E* fields at any location of interest, particularly those responsible for GIC in power grids.

One motivation for using this method is that *B* field measurements are only made at established observatories and additional installed locations. When only equation (6) is used, the *E* fields can only be computed at those locations from nearby conductivity profiles. By the inversion method, *B* fields can be computed over a section of the meridian close to these stations. Once the current strength is determined, one can return to the forward problem Fourier integral and use that parameter to calculate the *E* fields anywhere, not possible by other means [*De Villiers and Cilliers*, 2014]. Another motivation for computing ionospheric line currents by this method lies in the *B* field interaction with solar effects outside of the Earth's magnetosphere, such as the solar wind. The line current strength can be used as an intermediary parameter for modeling techniques that determine *B* fields at selected locations from the solar wind parameters. This simpler model provides an alternative method to estimate the currents in the ionosphere, which may be more amenable to modeling from upstream inputs for investigating storm characteristics all the way from the Sun to the Earth [*De Villiers et al*., 2016].

The dashed curves in Figures 3 to 5 are the *B* field measurements and forward calculated current strengths and *E* fields. The solid curves are the inverted *B* fields, modeled current strengths, and *E* fields. A cross correlation between the dashed and solid curves show that it equals an autocorrelation of either curve, indicating that they are identical. The results of the optimization problem match perfectly with the results directly obtained. This confirms that the geomagnetic model function of the line current system is correct. The dashed curves are exactly over the solid curves.

This study has implications for current and future research. The process of computing the current strengths and its *E* fields provides outputs in three different directions of research. The current density of equation (2) suggests that this work can be extended to distributions of currents, of which the Solar-quiet (*Sq*) current system is but one example. From scatter presentations, linear correlations and regressions can be performed between measured *B* field and modeled currents, or between measured d*B*/d*t* and modeled *E* field. From the inversion model, current strength data sets may be created for use to develop empirical models linking solar wind activity to magnetospheric current systems. The *E* fields are the input data for computing and predicting GIC in the various conductor-based networks on the ground at a given local region.

Appendix

The full profile given in *Omondi* [2013] and *Omondi et al*. [2014] has 21 layers and is reproduced here as comma-separated resistivities ρ_n (inverse conductivities $1/\sigma_n$) at corresponding depths d_n below Earth's surface (sum of successive thicknesses h_n), respectively:

$$\boldsymbol{d_n} = \Sigma \boldsymbol{h_n} = (3.2,\ 4,\ \underline{5}), (6.4,\ 8,\ 10,\ 12.6,\ 16,\ \underline{20}), (26,\ 32,\ 40,\ 50,\ 64,\ 70, \underline{80}),\ \underline{100},\ (126,\ \underline{160}),\ (200,\ \underline{260})\ \text{km};$$

$$\boldsymbol{\rho_n} = \frac{1}{\boldsymbol{\sigma_n}} = \begin{cases} (78.26,\ \underline{79.18},\ 77.26),\ (66.25,\ 62.91,\ \underline{52.82},\ 45.13,\ 38,\ 33.8),\ (30.74,\ 30.51, \\ 28.98,\ 33.32,\ 32.2,\ 25.9,\ \underline{29.74}),\ \underline{15.83},\ (40.13,\ \underline{44.55}),\ (46.8,\ \underline{58.08})\ \Omega\cdot\text{m}; \end{cases} \tag{A1}$$

The profile was simplified by combining the selected number of adjacent layers in parentheses into one layer, and taking the underlined values of resistivities as its new values. We tried to retain the shape of the profile as best we could in our selections (see Table 2).

Acknowledgments

The computed *EE* index relies on data collected at Addis Ababa and Huancayo. We thank Geophysical Observatory of Addis Ababa University, Institut de Physique du Globe de Paris (France), and Instituto Geofisico del Perú, for supporting its operation and INTERMAGNET for promoting high standards of magnetic observatory practice (www.intermagnet.org). The 1 min *Dst* index were downloaded at the National Geomagnetism Program of the U.S. Geological Survey (http://geomag.usgs.gov). The *SYM-H* and *AO* indices were downloaded at the World Data Center, Kyoto University (http://wdc.kugi.kyoto-u.ac.jp). The International Geomagnetic Reference Field (IGRF) model was used to obtain the geomagnetic coordinates at the same Kyoto WDC. The Apex coordinates was obtained at the Community Coordinated Modeling Center, Goddard Space Flight Center, National Aeronautics and Space Administration (http://ccmc.gsfc.nasa.gov/). We would like to thank Pierre Cilliers from the South African National Space Agency for his valuable input. All numerical information is provided in the figures produced by solving the equations in the paper. The authors are thankful to the reviewers for their careful editing of the text and helpful hints. This work was not funded. The authors declare no conflict of interest with respect to this work.

References

Alfven, H. (1939), A theory of magnetic storms and aurorae I, Kungliga Svenska Vetenskapsakademiens Handlingar (3), 18(3).

Alfven, H. (1940), A theory of magnetic storms and aurorae II, III, Ibid. 18(9).

Amm, O., and A. Viljanen (1999), Ionospheric disturbance magnetic field continuation from the ground to the ionosphere using spherical elementary current systems, *Earth Planets Space*, *51*, 431–440.

Anderson, D., and A. Anghel (2004), Daytime vertical E×B drift velocities inferred from ground-based magnetometer observations at low latitudes, *Space Weather*, *2*, S11001, doi:10.1029/2004SW000095.

Anderson, D., A. Anghel, K. Yumoto, M. Ishitsuka, and E. Kudeki (2002), Estimating daytime vertical ExB drift velocities in the equatorial F-region using ground-based magnetometer observations, *Geophys. Res. Lett.*, *29*(12), 1596, doi:10.1029/2001GL014562.

Anderson, D., A. Anghel, J. Chau, K. Yumoto, A. Bhattacharyya, and S. Alex (2006), Daytime, low latitude, vertical E×B drift velocities, inferred from ground-based magnetometer observations in the Peruvian Philippine and Indian longitude sectors under quiet and disturbed conditions; ILWS WORKSHOP 2006, GOA.

Barbosa, C., G. A. Hartmann, and K. J. Pinheiro (2015), Numerical modeling of geomagnetically induced currents in a Brazilian transmission line, *Adv. Space Res.*, *55*, 1168–1179.

Baumjohann, W., and R. A. Treumann (1996), *Basic Space Plasma Physics*, Imperial College Press, London.

Beland, J., and K. Small (2004), Space weather effects on power transmission systems: The cases of Hydro-Quebec and transpower NewZealand Ltd., in *Effects of Space Weather on Technology Infrastructure, Vol.176 of NATO Science Series, Ser. II: Mathematics, Physics and Chemistry*, edited by I. A. Daglis, pp. 287–299, NATO, Springer, Netherlands.

Bostrom, R. (1964), A model of the auroral electrojets, *J. Geophys. Res.*, *69*(23), 4983, doi:10.1029/JZ069i023p04983.

Boteler, D. H., and R. J. Pirjola (1998), The complex-image method for calculating the electric and magnetic fields produced at the surface of the Earth by the auroral electrojets, *Geophys. J. Int.*, *132*, 31–40.

Boteler, D. H., R. J. Pirjola, and L. Trichtchenko (2000), On calculating the electrical and magnetic fields produced in technological systems at the Earth's surface by a "wide" electrojets, *J. Atmos. Sol.-Terr. Phys.*, *62*, 1311–1315.

Bothmer, V., and I. A. Daglis (Eds) (2007), *Space Weather—Physics and Effects*, Springer, Praxis Ltd., Chichester, U. K.

Cagniard, L. (1953), Basic theory of the magnetotelluric method of geophysical prospecting, *Geophysics*, *18*, 605–635.

Carter, B. A., E. Yizengaw, R. Pradipta, A. J. Halford, R. Norman, and K. Zhang (2015), Interplanetary shocks and the resulting geomagnetically induced currents at the equator, *Geophys. Res. Lett.*, *42*, 6554–6559, doi:10.1002/2015GL065060.

Casey, J. P. (2005), Overview of the equatorial electrojet and related ionospheric current systems NUWC-NPT Tech. Rep., 11, 676.

Civet, F., E. Thébault, O. Verhoeven, B. Langlais, and D. Saturnino (2015), Electrical conductivity of the Earth's mantle from the first Swarm magnetic field measurements, *Geophys. Res. Lett.*, *42*, 3338–3346, doi:10.1002/2015GL063397.

Danskin, D. W., and S. I. Lotz (2015), Analysis of geomagnetic hourly ranges, *Space Weather*, *13*, 458–468, doi:10.1002/2015SW001184.

Davis, T. N., and M. Sugiura (1965), Auroral electrojet activity index AE and its universal time variation, NASA Goddard Space Flight Center.

De Villiers, J. S., and P. J. Cilliers (2014), Applying inversion techniques to derive source currents and E-fields for geomagnetically induced current calculations, *Ann. Geophys.*, *32*, 1263–1275, doi:10.5194/angeo-32-1263-2014.

De Villiers, J. S., R. J. Pirjola, and P. J. Cilliers (2016), Estimating ionospheric currents by inversion from ground-based geomagnetic data and calculating geoelectric fields for studies of geomagnetically induced currents, *Earth Planets Space*, *68*, 154, doi:10.1186/s40623-016-0530-1.

Egedal, J. (1947), The magnetic diurnal variation of the horizontal force near the magnetic equator, *Terr. Magn. Atmos. Electr.*, *52*(4), 449–451, doi:10.1029/TE052i004p00449.

Gannon, J. L., and J. J. Love (2011), USGS 1-min Dst index, *J. Atmos. Sol.-Terr. Phys.*, *73*, 323–334.

Gaunt, C. T., and G. Coetzee (2007), Transformer failures in regions incorrectly considered to have low GIC-risk, in *Proceedings of IEEE Power Technology; Conference*, pp. 1–6, IEEE Press, Lausanne, Switzerland.

Gilbert, W. (1600), *De Magnete, Magneticisque Corpori bus, et de Magno Magnete Teilure (English: On the Magnet and Magnetic Bodies, and on that Great Magnet the Earth)*, Dover Pub., New York.

Häkkinen, L., and R. Pirjola (1986), Calculation of electric and magnetic fields due to an electrojet current system above a layered Earth, *Geophysica*, *22*(1-2), 31–44.

Iyemori, T. (1990), Storm-time magnetospheric currents inferred from midlatitude geomagnetic field variations, *J. Geomagn. Geoelectr.*, *42*, 1249.

Kappenman, J. G. (2007), Geomagnetic disturbances and impacts upon power system operation, in *The Electric Power Engineering Handbook*, 2nd ed., edited by L. L. Grigsby, chap. 16, pp. 16–22, CRC Press/IEEE Press, Boca Raton, Fla.

Kerridge, D. (2001), INTERMAGNET: Worldwide near-real-time geomagnetic observatory data, in *Proceedings of the Workshop on Space Weather*, p. 34, ESTEC, Noordwijk, Neth. [Available at www.intermagnet.org/publications/IM_ESTEC.pdf (last access: 7 July 2014).]

Kozyra, J. U., and M. W. Liemohn (2003), Ring current energy input and decay, *Space Sci. Rev.*, *109*(1–4), 105–131, doi:10.1023/B:SPAC.0000007516.10433.ad.

Liu, C., Y. Li, and R. Pirjola (2014), Observations and modeling of GIC in the Chinese large-scale high-voltage power networks, *J. Space Weather Space Clim.*, *4*, A03, doi:10.1051/swsc/2013057.

Lourakis, M. I. A. (2005), *A Brief Description of the Levenberg-Marquardt Algorithm Implemented by Levmar*, Inst. of Comput. Sci., Found. for Res. and Technol., Hellas, Greece.

Love, J. J., and A. Swidinsky (2015), Observatory geoelectric fields induced in a two-layer lithosphere during magnetic storms, *Earth Planets Space*, *67*, 58, doi:10.1186/s40623-015-0213-3.

Marshall, R. A., M. Dalzell, C. L. Waters, P. Goldthorpe, and E. A. Smith (2012), Geomagnetically induced currents in the New Zealand power network, *Space Weather*, *10*, S08003, doi:10.1029/2012SW000806.
Ngwira, C. M., A. Pulkkinen, F. D. Wilder, and G. Crowley (2013), Extended study of extreme geoelectric field event scenarios for geomagnetically induced current applications, *Space Weather*, *11*, 121–131, doi:10.1002/swe.20021.
Omondi, G. (2013), MSc Thesis, Maseno Univ.
Omondi, G., B. Ndinya, and P. Baki (2014), Signatures of low-latitude geomagnetically induced currents effects on transformers in Nairobi, Kenya, in *Proceedings of the Workshop on GICs in Power Systems With Emphasis on Mid- and Low-Latitude Regions*, pp. 7–8, Univ. of Cape Town, South Africa.
Onwumechili, C. A. (1998), *The Equatorial Electrojet*, CRC Press, Amsterdam.
Owen, M. (2007), *Practical Signal Processing*, Cambridge Univ. Press, Cambridge, England.
Pirjola, R. (1982), Electromagetic induction in the Earth by a plane wave or by fields of line currents harmonic in time and space, *Geophysica*, *18*(1), 001.
Pirjola, R. (1984), Estimation of the electric field on the Earth's surface during a geomagnetic variation, *Geophysica*, *20*(2), 089.
Pirjola, R. (1985), Electromagetic induction in the Earth by a line current harmonic in time and space, *Geophysica*, *21*(2), 127.
Pirjola, R. (1998), Modelling the electric and magnetic fields at the Earth's surface due to an auroral electrojets, *J. Atmos. Sol.-Terr. Phys.*, *60*, 1139–1148.
Pirjola, R., and D. Boteler (2002), Calculation methods of the electric and magnetic fields at the Earth's surface produced by a line current, *Radio Sci.*, *37*(3), 1042, doi:10.1029/2001RS002576.
Pirjola, R., and A. Viljanen (1998), Complex image method for calculating electric and magnetic fields produced by an auroral electrojet of finite length, *Ann. Geophys.*, *16*, 1434–1444.
Press, W. H., S. A. Teukolsky, W. T. Vetterling, and B. P. Flannery (1992), *Numerical Recipes*, Cambridge Univ. Press, Cambridge, England.
Pulkkinen, A. (2003), Geomagnetic induction during highly disturbed space weather conditions: Studies of ground effects, Thesis at the Finnish Meteorol. Inst.
Pulkkinen, A., O. Amm, A. Viljanen, and B. E. A. R. Working Group (2003), Ionospheric equivalent current distributions determined with the method of spherical elementary current systems, *J. Geophys. Res.*, *108*(A2), 1053, doi:10.1029/2001JA005085.
Pulkkinen, A., R. Pirjola, and A. Viljanen (2007), Determination of ground conductivity and system parameters for optimal modeling of geomagnetically induced current flow in technological systems, *Earth Planets Space*, *59*, 999–1006.
Pulkkinen, A., E. Bernabeu, J. Eichner, C. Beggan, and A. W. P. Thomson (2012), Generation of 100-year geomagnetically induced current scenarios, *Space Weather*, *10*, S04003, doi:10.1029/2011SW000750.
Richmond, A. D. (1995), Ionospheric electrodynamics using magnetic Apex coordinates, *J. Geomagn. Geoelectr.*, *47*, 191–212.
Schwarz, G., and D. Kruger (1997), Resistivity cross section through the southern central Andes as inferred from magnetotelluric and geomagnetic deep soundings, *J. Geophys. Res.*, *102*(B6), 11,957–11,978, doi:10.1029/96JB03626.
Sugiura, M. (1964), Hourly values of equatorial Dst for the IGY, *Ann. Int. Geophys. Year*, *35*, 9–45.
Thomson, A. W. P., A. J. McKay, E. Clarke, and S. J. Reay (2005), Surface electric fields and geomagnetically induced currents in the Scottish Power grid during the 30 October 2003 geomagnetic storm, *Space Weather*, *3*, S11002, doi:10.1029/2005SW000156.
Thomson, A. W. P., E. B. Dawson, and S. J. Reay (2011), Quantifying extreme behavior in geomagnetic activity, *Earth Planets Space*, *9*, S10001, doi:10.1029/2011SW000696.
Thomson, D. J., and J. T. Weaver (1975), The complex image approximation for induction in a multilayered Earth, *J. Geophys. Res.*, *80*(1), 123–129, doi:10.1029/JA080i001p00123.
Torta, J. M., L. Serrano, J. R. Regué, A. M. Sánchez, and E. Roldán (2012), Geomagnetically induced currents in a power grid of northeastern Spain, *Space Weather*, *10*, S06002, doi:10.1029/2012SW000793.
Trivedi, N., et al. (2007), Geomagnetically induced currents in an electric power transmission system at low latitudes in Brazil: A case study, *Space Weather*, *5*, S04004, doi:10.1029/2006SW000282.
Uozumi, T., et al. (2008), A new index to monitor temporal and long-term variations of the equatorial electrojet by MAGDAS/CPMN real-time data: EE-Index, *Earth Planets Space*, *60*, 785–790.
Vanhamäki, H., and O. Amm (2007), A new method to estimate ionospheric electric fields and currents using data from a local ground magnetometer network, *Ann. Geophys.*, *25*, 1141–1156.
Vanhamäki, H., O. Amm, and A. Viljanen (2003), One-dimensional upward continuation of the ground magnetic field disturbance using spherical elementary current systems, *Earth Planets Space*, *55*, 613–625.
Viljanen, A. (1992), Geomagnetic induction in a one- or two-dimensional Earth due to horizontal ionospheric currents, Thesis at the Finnish Meteorol. Inst.
Viljanen, A., A. Pulkkinen, O. Amm, R. Pirjola, and T. Korja (2004), Fast computation of the geoelectric field using the method of elementary current systems and planar Earth models, *Ann. Geophys.*, *22*(1), 101–113.
Wait, J. A. (1958), Transmission and reflection of electromagnetic waves in the presence of stratified media, *J. Res. Natl. Bur. Stand.*, *61*(3), 205–232.
Wait, J. A. (1980), Electromagnetic surface impedance for a layered Earth for excitation, *Radio Sci.*, *15*(1), 129–134, doi:10.1029/RS015i001p00129.
Wait, J. R., and K. P. Spies (1969), On the representation of the quasi-static fields of a line current source above the ground, *Can. J. Phys.*, *47*(23), 2731–2733.
Wanliss, J. A., and K. M. Showalter (2006), High-resolution global storm index: Dst versus SYM-H, *J. Geophys. Res.*, *111*, A02202, doi:10.1029/2005JA011034.
Watari, S. (2015), Estimation of geomagnetically induced currents based on the measurement data of a transformer in a Japanese power network and geoelectric field observations, *Earth Planets Space*, *67*, 77, doi:10.1186/s40623-015-0253-8.
Watari, S., et al. (2009), Measurements of geomagnetically induced current in a power grid in Hokkaido, Japan, *Space Weather*, *7*, S03002, doi:10.1029/2008SW000417.
Wik, M., A. Viljanen, R. Pirjola, A. Pulkkinen, P. Wintoft, and H. Lundstedt (2008), Calculation of geomagnetically induced currents in the 400 kV power grid in southern Sweden, *Space Weather*, *6*, S07005, doi:10.1029/2007SW000343.
Zhang, J. J., C. Wang, T. R. Sun, C. M. Liu, and K. R. Wang (2015), GIC due to storm sudden commencement in low-latitude high-voltage power network in China: Observation and simulation, *Space Weather*, *13*, 643–655, doi:10.1002/2015SW001263.